EPSC2018

LSE5 abstracts

EPSC Abstracts
Vol. 12, EPSC2018-331, 2018
European Planetary Science Congress 2018

Enhancements in the lunar exosphere seen in LACE data

Rosemary M. Killen (1), David R. Williams (1), Jaekyun Park (2), Orenthal J. Tucker (1), Sang-Joon Kim (2)
(1) NASA Goddard Space Flight Center, Greenbelt, MD, USA, (2) School of Space Research, Kyung Hee University, Republic of Korea. (rosemary.killen@nasa.gov)

Abstract

Apollo 17 carried a miniature mass spectrometer, called the Lunar Atmospheric Composition Experiment (LACE), to the Moon as part of the Apollo Lunar Surface Experiments Package (ALSEP) to study the composition and variations in the lunar atmosphere [4]. Although our initial task was to archive the LACE data in the Planetary Data System, during this analysis a sudden increase in many, but not all, of the atomic species was discovered during the 5th lunation. The solar wind plasma flux was elevated during the entire 10 hour period preceding the enhancements in exospheric density observed by LACE. The maximum in the solar wind plasma flux during this time period was measured by the IMP-6 spacecraft in Earth orbit at 20:00 hours on May 6, about four hours prior to the observed density enhancement on the nightside. Our Monte Carlo models cannot reproduce the observed sudden increase with the increase in the solar wind flux at the Moon. Alternative explanations may involve a small meteoroid impact.

1. Introduction

The LACE data were available for mass/charge (M/Q) 1 to 100, but the usable data are in the range 16 - 45 AMU/Q. The raw data are in counts per 0.6 second. The first task was therefore to calibrate the data. There is no available calibration for the LACE mass spectrometer data, however, a similar instrument was constructed and flown on the Pioneer Venus mission [3] and we used their calibration. Looking closely at the variation of the Mass 22 peak over the 9 available lunations, a sudden increase of peak in the later part of 5th lunation was seen. Although the second half of 5th lunation was mostly noise, a mass 22 peak suddenly appeared at 00.38 UT on May 7th, 1973. We then saw that the other masses were increased, but by varying amounts (Figure 1). We show in Table 1 the ^{20}Ne densities estimated from the Pioneer Venus neutral mass spectrometer calibration curve.

1.1 Solar Wind Data

We saw an enhancement in ^{20}Ne of a factor of 18.4 on May 7, 1973, from 00 UT to 01 UT, then decreasing for 8 - 10 hours. Solar wind data for this time period obtained by the IMP-6 spacecraft, which was in Earth orbit during years 1971-1974, were retrieved from the NASA OMNIWeb [5, 7] for IMF (B (nT)), proton density, n (cm^{-3}), solar wind velocity, v (km/s), and alpha/proton ratio. The solar wind plasma flux was elevated during the entire 10 hour period preceding the enhancements in exospheric density observed by LACE. The increase in exospheric densities began about 00 UT on May 7, 1973 after the proton flux had been elevated for the 10 hour period preceding this observation. Although the solar wind speed increased to 600 km/s 12 hours later, the proton density decreased to about 3 cm^{-3}, and the proton flux would have been reduced by an order of magnitude below that seen just before our observation of elevated exospheric density. The maximum flux was 1.76 x10^{9} protons cm^{-2} s^{-1}, and it remained high throughout the period leading up to our observations on May 7, 00 hours UT, when the plasma flux was 7.58 x10^{8} protons cm^{-2} s^{-1}.

2. Figure and Table

Figure 1: Increase ratio for M/Q 15 - 50

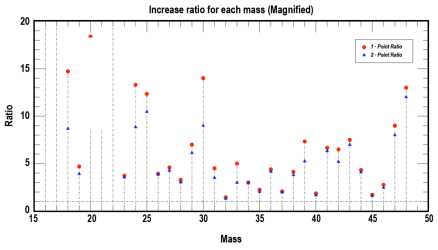

Table 1: ^{20}Ne densities estimated for lunations 2 - 5

Lunation	^{20}Ne Density atoms/cm^3
2nd	1.5 - 3.5 x 10^3
3rd	2.0-4.5 x 10^3
4th	2.0- 4.0 x 10^3
5th before &after	2.0 - 4.0 x10^3
5th increased	2.74 x10^4

3. Summary and Conclusions

We have observed a measured increase in ^{20}Ne at the Moon observed on May 7, 1973, at 00 Hr UT after an elevated solar wind flux observed by the IMP6 spacecraft. The measured ^{20}Ne densities before and after the solar wind increase were consistent with the ^{20}Ne column densities reported by Cook et al. (2013) [2] for normal solar wind conditions and by Benna et al. (2015) [1] for CME conditions, respectively. The Benna et al. (2015) value was measured during the CME of 7-27 Feb. 2014. For CME conditions, the solar wind would have an enhanced abundance of heavy ions such that Ne/O =0.32 and O/H=3x10^{-4} [6]. If v_{sw}=800 km/s and N_{sw}=10 cm^{-3} as expected for the CME, then the solar wind Ne flux to the lunar surface would be Ne = 7.7x10^4 cm^{-2} s^{-1}. If we assume CME conditions persisted for 4.5 days, the column abundance at the subsolar point would be N(Ne)=3x10^{10} cm^{-2}. We have not been able to reproduce the measured rapid increase and rapid decline in ^{20}Ne seen in the LACE data with our Monte Carlo model [8] using the measured solar wind flux. It is possible that the increased density was the result of an impact on the lunar nightside. We believe that the increase in surface number density at mass 22 at sunrise is not ^{22}Ne but rather CO_2^{++}. If Ne were evaporating at dawn the surface number density would decrease, not increase since the scale height would be increasing. Ne is a non-condensable gas. Thus the increased counts at dawn are not Ne but a contaminant, most likely CO_2^{++}. A dawn increase at Mass 20 could be MgO^{++}, Ar^{++}or Ca^{++} as well as ^{20}Ne. We also see an increase in oxygen and hydroxyl at the same time as the increase in Ne. These values will be considered in a subsequent paper.

Acknowledgements

RMK was funded by the DREAM2 Team of NASA's SSERVI. JP and S-JK acknowledge support from the Space Core Technology program through NRF funded by the Ministry of Education, Science and Technology, Republic of Korea. We acknowledge use of NASA/GSFC's Space Physics Data Facility's OMNIWeb and OMNI data.

References

[1] Benna, M., et al.: Variability of helium, neon, and argon in the lunar exosphere as observed by the LADEE NMS instrument, Geophys. Res. Lett., Vol. 42 #10, pp. 3723-3729, 2015.

[2] Cook, J. C., et al.: New upper limits on numerous atmospheric species in the native lunar atmosphere, Icarus, Vol. 225, pp. 681-687, 2013.

[3] Donahue, T. and Hodges, R.: 1992. Past and present water budget of Venus. Journ. Geophys.Res. Vol. 97 E4, pp. 6083-6091, 1992.

[4] Hoffman, J. H.: Lunar Atmospheric Composition Experiment Final Report June 1, 1971- September 30, 1975. NAS 9-12074, 1975.

[5] King, J. H. and Papatashvilli., N.: Plasma Data from cohoweb. CDAWeb, Adnet Systems, NASA Goddard Space Flight Center, Greenbelt MD. Generated Feb. 15, 2018.

[6] Shearer, P., et al.: The solar wind neon abundance observed with ACE/SWICS and Ulysses/SWICS, Astrophysical Journal, 789, pp. 60, 2014.

[7] Smith, E. J. and Barnes., A.: CDAWeb, NASA JPL/AMES, 2018.

[8] Tucker O.J. et al.: Solar Wind implantation into lunar regolith II: Monte Carlo simulations of hydrogen retention in a surface with defects and the hydrogen (H2) exosphere,49th LPSC, 2018.

EPSC Abstracts
Vol. 12, EPSC2018-450, 2018
European Planetary Science Congress 2018

Estimating sub-pixel lunar block distributions

S.M. Klem, M.S. Robinson, and the LROC Science Team
Arizona State University, Arizona, USA (sklem@ser.asu.edu)

1. Introduction

Block size-frequency distributions (BSFDs) provide insight to the ejecta and surface roughness in and around craters, and serve as a proxy for the physical state of the substrate [1-4]. This study investigates BSFD (>2.5-m) and how accurately the BSFD can be extrapolated to smaller diameters (down to 10-cm).

Block populations were identified from Lunar Orbiter (LO), Surveyor III (SIII), Chang'E-3 (CE-3), and Lunar Reconnaissance Orbiter Camera (LROC) Narrow Angle Camera (NAC) images (LO [2], SIII [11], CE-3 [3]). Since available pixel scale limits our ability to identify sub-meter scale blocks, our understanding of block distributions down to the 10-cm scale is incomplete – this size range is critical for the interpretation of Mini-RF radar observations [13]. Mini-RF has two modes, S-band (12.6-cm) and X-band (4.2-cm) [13]. In the S-band observations, some polar crater interiors have radar backscatter anomalies with high circular polarization ratios (CPRs) and low CPR for their exteriors, these craters are referred to as anomalous craters [4, 12-13]. Small blocks with diameters near the wavelength of the radar signal [13] and ice are both potential sources of the high-CPR signals [4]. Accurate estimates of the 10-cm block population allow testing of the ice or blockiness hypotheses for the high-CPR signals seen in the anomalous craters.

The NAC pixel scale is 0.5-m (from an altitude of 50-km), which allows for confident identification and measurement of blocks >2.5-m in diameter. The goal of this work is to determine the accuracy of extrapolating from >2.5-m diameter block populations down to 10-cm diameter.

Testing the ice vs. blockiness hypotheses for the anomalous craters is critical for constraining the lunar polar volatile inventory. Currently there are no orbital datasets with the proper pixel scale, so we are stuck with extrapolating from meter-sized blocks visible in orbital images from the NAC (and those to be acquired by ShadowCam, pixel scale of 1.7-m at an orbit of 100-km [10]).

2. Background

Previous studies, determining block populations for potential landing sites on Mars [5-9], compared block populations and how meter and sub-meter-sized blocks are related. They proposed that larger diameter block populations (>1.5-m) can be accurately extrapolated down to 10-cm scales [8], but if the counts were limited to >5-m blocks, the extrapolation accuracy diminished [7]. A lower limit for extrapolation for Mars lends some degree of confidence for similar results at the Moon.

Lunar block populations across a broad size range were derived from LO (>2-m diameters) and SIII images (0.001 to 0.3-m diameters) [2, 11]. Cumulative SFD of the block counts both had negative slopes but the LO slope (blocks 2 to 6.3-m) was steeper than the SIII slope (blocks 0.001 to 0.251-m.) The steeper, negative slope for meter-sized blocks overestimates the number of sub-meter blocks. The difference in slope could mean the population of blocks changes.

Cintala and McBride [2] compared LO coverage of several Surveyor landing sites to the work done by Shoemaker and Morris [11]. From the plots it was found that the Surveyor III site was the closest matched between the SIII and LO counts [2]. More recently, block populations were determined from NAC [6, 14] orbital images and CE-3 surface images [3]. The BSFD also showed roll over as the block size approached the resolution cut off.

3. Method

The maximum diameter was recorded for the blocks [5], as was done for the LO counts [2]. Block counts from a NAC image covering a similar area used for the LO image for the Surveyor III site [2] for analysis. The cut off for the blocks in the NAC image is 2.5-m since the pixel scale for the image is 0.5-m. The new block counts were binned to match the data from Cintala and McBride [2]. The data was plotted on a log-log scale with a power law applied for fitting.

The data for the NACs, Chang'E-3 LCAM, and LO were cut off at 5 times the pixel scale of the image avoiding plotting past the confidence limit of block diameters.

3.1 Block Count Sites

Four sites were selected for this study. Surveyor III (Fig. 1) and the CE-3 (Fig. 2) landing sites were selected to compare with previous work, which included block counts from surface images, allowing direct comparisons between the sub-meter population and the meter population. Block counts were derived from one NAC pair for each site and three CE-3 LCAM descent images.

The two other sites selected were a block field on a low altitude NAC image with pixel dimensions of 0.21 x 0.57-m and processed at 0.2-m pixel scale. This image provided a BSFD with a larger block count area than those of the CE-3 descent images (see Fig 2). A newly formed (October 2012) 70-m impact crater provided an example of the block population around a fresh impact crater.

4. Results

Slope values for the LO [2] and NAC BSFDs are similar but both differ from the SIII slope (Fig. 1). Image resolution and counting errors could contribute to the difference in slopes or, variations in the degradation rate of blocks and thus predicted survival times [1]. Overhead block counts for the CE-3 sites (NAC and CE-3 descent camera) were compared to block counts from the Yutu rover NavCam images [3]. The Chang'E-3 descent LCAM image counts bridge part of the sub-meter to meter block gap (Fig. 2). Yutu NavCam based BSFD [3] has a different slope likely due to the small area and non-representative area imaged by the rover. The slopes for two of the Chang'E-3 LCAM counts (black and purple markers in Fig. 2) match up with the slope from the NAC count, indicating that extrapolation from >2.5-m population to sub-meter blocks is possible.

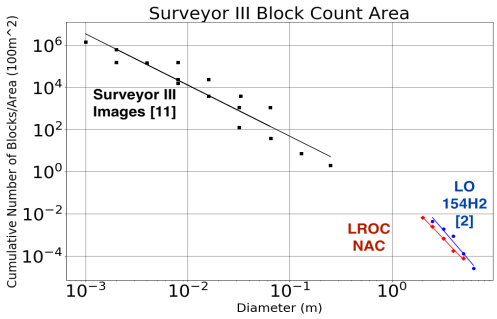

Figure 1: Log plot of size-frequency distribution of block counts for Surveyor III landing site.

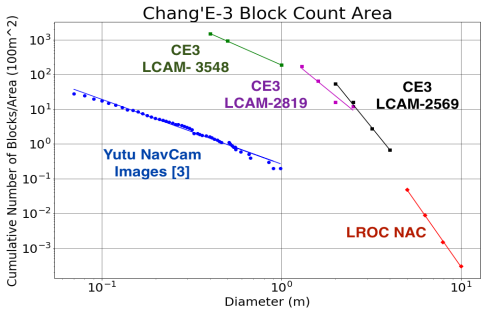

Figure 2: Log plot of size-frequency distribution of block counts for Chang'E-3 landing site.

4. Future Work

Additional comparisons of meter and sub-meter scale block populations are needed to allow more confident extrapolations to smaller diameters from larger diameters. Until high-resolution orbital images are available such extrapolations are required to assess the nature of high-CPR backscatter seen in and out of PSRs and in turn help constrain the lunar polar volatiles inventory.

References

[1] Basilevsky A. T. et al., *Planet. & Space Sci. 89*, 118-126, 2013. [2] Cintala, M.J. and McBride K. M., *NASA Tech. Mem,* 1995. [3] Di K. et al., *Planet. & Space Sci. 120,* 103-112, 2015. [4] Ghent R. R. et al., Icarus, 273, 182-195, 2016. [5] Kneissl T. et al., Planet*. & Space Sci.59,* 1243-1254, 2010. [6] Golombek M. P. et al., JGR*, 103,* 4117-4129, 1997. [7] Golombek M. P. et al., *JGR, 108,* E12, 2003a. [8] Golombek M. P. et al., *JGR, 113,* E00A09, 2008a. [9] Golombek M. P e. Al., *Mars J., 7,* 1-22, 2012. [10] Robinson M. S. et al., EPSC*, 11,* 2017. [11] Shoemaker E. M. & Morris E. C., *Surveyor Project Final Report Part II,* 86-102, 1968. [12] Spudis P. D. et al., *GRL, 37,* L06204, 2010. [13] Spudis P. D. et al., *GRL, 118,* 2016-2029, 2013. [14] Yuan L. et al., *Planet. & Space Sci.,* 1-10, 2017.

EPSC Abstracts
Vol. 12, EPSC2018-530, 2018
European Planetary Science Congress 2018

Probing the volatile reservoirs in the Moon using lunar meteorites

A. Stephant[1], H. O. Ashcroft[1], M. Anand[1,2], I.A. Franchi[1], X. Zhao[1], R.L. Korotev[3], R.C. Greenwood[1], S. Strekopytov[4], E. Humphreys-Williams[4], S. Hu[5], Y. Liu[6], G. Tang[6], Q. Li[6].
[1]School of Physical Sciences, The Open University, Milton Keynes, UK. (alice.stephant@open.ac.uk); [2]Department of Earth Sciences, The Natural History Museum, London, UK; [3]Department of Earth & Planetary Sciences and McDonnell Center for the Space Sciences, Washington University, Saint Louis MO 63130; [4]Imaging and Analysis Centre, The Natural History Museum, London, UK; [5] Key Laboratory of Earth and Planetary Physics, Institute of Geology and Geophysics, CAS, Bejing, China; [6] State Key Laboratory of Lithospheric Evolution, Institute of Geology and Geophysics, CAS, Bejing, China

Abstract

1. North West Africa (NWA) 10989 is a lunar meteorite found in 2014. Petrology, bulk chemistry and mineralogy of NWA 10989 are consistent with it being an intermediate-iron meteorite, consisting of ~40% mafic nonmare material and 60% of very low Ti basalt material, with no obvious KREEP component. Analyses of chlorine and hydrogen isotopic composition and abundances of apatite grains support sampling of 2 distinct reservoirs, one being similar to those for known mare-basalts in Apollo collections, while the other could represent a yet unrecognized reservoir, which doesn't fit in existing H-Cl systematics of lunar samples. In situ Th-U-Pb dating reveals that phosphates represent two distinct ages with one ranging from 3.98 to 4.20 Ga, while the other are from 3.32 to 3.96 Ga, the latter being more similar to ages of basalts known from Apollo collections. This unique lunar breccia features mixing of material, which doesn't appear to have been recorded by Apollo samples. Consequently, we propose that NWA 10989 originated from a mare-highlands boundary, possibly on the lunar farside.

2. Introduction

The majority of lunar meteorites are thought to originate from different areas on the Moon to those which the Apollo and Luna missions visited, providing broader coverage across the Moon's surface of both the nearside and the farside. Therefore, lunar meteorites expand our knowledge of the surface composition of the Moon, and enhance our understanding of the bulk composition of the Moon and its evolution through history. Brecciated meteorites contain a variety of clast types and geochemical information providing a snapshot into the mixing processes which occur at a local scale, and the diversity of material which is present at a single location.

1.1 Lunar Meteorite NWA 10989

NWA 10989 is a lunar meteorite that was found near the Morocco/Algeria border in 2014. NWA 10989 is a single, roughly spherical stone with a diameter of ~2 cm and a mass of 14.41 g with a dark brown fusion crust. Based on an initial petrographic and geochemical investigation it was classified as an intermediate ('mingled') iron, lunar fragmental breccia. It is composed of mare- and highlands-derived materials in roughly equal proportions.

3. Methodology

This study presents a comprehensive mineralogical and geochemical data on mineral, lithic and impact melt clasts in this meteorite including its bulk-rock major- and trace-element composition, abundance and isotopic composition of chlorine and hydrogen and Pb-Pb dates in apatite. This new dataset is then utilized to perform comparisons with other lunar samples in order to gain insights into important lunar petrogenetic processes and evaluate potential source region(s) for NWA 10989.

4. Major Findings

There are several points to take into account for inferring the origin of NWA 10989 on the Moon:

1) NWA 10989 is an intermediate meteorite composed of materials from two distinct compositional sources – a magnesian highlands, not represented in Apollo or Luna collections, and a VLT-like basaltic material similar to Apollo 17 and Luna 24 mare basalts.

2) There is no lithological evidence for KREEP, despite the 'Apollo Model' mass balance suggesting up to 3 % KREEP, with 45 % mare material and 52 % feldspathic material. Indeed, all Apollo breccias consisting mainly of anorthosite and basalt also contain a little bit of KREEP, contrary to binary anorthosite-basaltic meteorites (i.e.YQEN group, MET 01210, Dhofar 1180 and NWA 3136). The 'Apollo model' does not distinguish between mare basalts and mafic lithologies which may occur within highlands rocks. As such, the incompatible elements may be supply by this mafic nonmare component, supported by the presence of ultramafic peridotite clasts; component which doesn't exist in the Apollo samples. Therefore, a significant proportion of the mafic material appears to be associated with felsdpathic material which is s. As a result, NWA 10989 derive from a region quite distant from the Procellarum KREEP rich Terrane.

3) δD and δ^{37}Cl analyses of NWA 10989 apatites show a strong resemblance with the KREEP rich breccia NW 4472. However, as just stated previously, NWA 10989 does not contain any significant KREEP-rich material. Combined analyses of δD-δ^{37}Cl with age dating of apatites highlight two groups of apatites: one group which sampled a typical mare basalt source (i.e. δD>400‰, δ^{37}Cl~15‰), while the other group sampled an unusual basaltic reservoir, with hydrogen isotopic composition as low δD as -433 ‰, similar to older Mg-suite rocks from Apollo collections but whose chlorine isotope signature is more akin to younger mare basalts. This evidence strongly argues for the presence of material in this breccia, which is either not yet identified in the Apollo collections or more likely represents an area of the Moon not sampled by the Apollo missions.

4) There is a variety of evidence suggesting that material from this rock did not come from the very surface layer of the moon, but slightly deeper in the crust. Indeed, the 1-2 μm thick exsolution lamellae in pyroxene, the presence of peridotite clasts that formed at high pressure-temperature, as well as the abundance of coarse-grained minerals, all suggesting a slow cooling regime. The various scenarios compatible with this slow-cooling could be a crustal intrusion, thick lava flow, hypabyssal setting or burial beneath a thick layer of hot ejecta from a basing scale crater like in a cryptomare region.

5) The effects of several impacts can be witnessed throughout this rock. The minerals and impact melt clasts show varying degrees of shock, with the maskelynitisation of certain plagioclase and shock crystallization textures in some other plagioclases. The range of impact melt clasts are likely to have formed closer to an impact crater than the reworked basalts, in order for higher temperatures and metamorphism to be reached.

6) As implied by its binary nature, NWA 10989 probably originated like other felsdpathic-mare intermediate-iron breccias from a region of the Moon where mare basalt has mixed with felsdpathic highland terrane. Mare-highland boundaries do exist on the lunar nearside, potentially close to the Luna 24 or Apollo 17 landing sites where VLT basalts have been found. However, some chemical features of NWA 10989 are incompatible with this possibility. First, the more mafic nature of the felsdpathic material in NWA 10989 compared to Apollo anorthositic highlands material argue for mafic nonmare component quite distinct from the FHT material sampled by Apollo missions. Secondly, the lack of KREEP component and high Ti mare material places this breccia far from the PKT, and again far from Apollo landing sites. As a result, the more probable source location for this breccia would be on a maria-highlands boundary on the farside.

Acknowledgements: We thank Graham Ensor for providing us this fascinating lunar meteorite. MA and IAF acknowledge funding from Science and Technology Facilities Council (STFC) grants (#ST/I001964/1 and #ST/L000776/1).

EPSC Abstracts
Vol. 12, EPSC2018-729, 2018
European Planetary Science Congress 2018

Mini-RF S- and X-band Bistatic Observations of South Polar Craters on the Moon

G. W. Patterson (1), P. Prem (1), A. M. Stickle (1), J. T. S. Cahill (1), Land the Mini-RF Team
(1) Johns Hopkins University Applied Physics Laboratory, Laurel, MD (Wes.Patterson@jhuapl.edu).

Abstract

Mini-RF S-band bistatic observations of Cabeus crater floor materials display a clear opposition response consistent with the presence of water ice. Initial X-band bistatic observations of Cabeus and Amundsen crater floor materials do not show a similar response. This could indicate that, if water ice is present in Cabeus crater floor materials, it is buried beneath ~0.5 m of regolith that does not include radar-detectible deposits of water ice.

1. Introduction

Mini-RF aboard NASA's Lunar Reconnaissance Orbiter (LRO) is a hybrid dual-polarized synthetic aperture radar (SAR). Its receiver operates in concert with transmitters at either the Arecibo Observatory (AO) or the Goldstone deep space communications complex 34 meter antenna DSS-13 to collect S- and X-band bistatic radar data of the Moon, respectively [1]. Bistatic radar data provide a means to probe the near subsurface for the presence of water ice, which exhibits a strong response in the form of a Coherent Backscatter Opposition Effect (CBOE). Here we present S- and X-band bistatic radar observations for the floors of the south-polar craters Cabeus and Amundsen and discuss their potential for harboring water ice.

2. Background

Radar observations of planetary surfaces provide important information on the structure (i.e., roughness) and dielectric properties of surface and buried materials [2-5]. A common product used in the analysis SAR data is the Circular Polarization Ratio (CPR). CPR is a representation of surface roughness at the wavelength scale of the radar. Surfaces that are smoother at the wavelength scale will have lower CPR values and surfaces that are rougher will have higher CPR values. High CPR values can also serve as an indicator of the presence of water ice.

Laboratory data and analog experiments at optical wavelengths have shown that the scattering properties of lunar materials (e.g., CPR) can be sensitive to variations in phase angle [6-8]. This sensitivity manifests as an opposition effect and likely involves contributions from shadow hiding at low angles and coherent backscatter near 0°. Analog experiments and theoretical work have shown that the scattering properties of water ice are also sensitive to variations in phase angle, with an opposition effect that it is tied primarily to coherent backscatter [9-11]. Differences in the character of the opposition response of these materials offer an opportunity to differentiate between them, an issue that has been problematic for radar studies of the Moon that use a monostatic architecture [12,13].

3. Observations

Mini-RF bistatic observations of south polar crater floors currently include Cabeus (84.9°S, 35.5°W; 98 km dia.) and Amundsen (84.5°S, 82.8°E; 103 km dia.). Mini-RF monostatic data of the craters does not show evidence for radar-detectible deposits of water ice in the top meter(s) of the surface [e.g., 14]. However, an initial Mini-RF bistatic observation of the crater showed scattering characteristics for its floor that differed from the surrounding terrain [15]. Cabeus was targeted at S-Band on 4 subsequent occasions but a ground issue at AO limited the collection of data for one of the observations to regions outside the crater floor. The purpose of those observations was to provide additional data on the scattering characteristics of its floor materials and to characterize and compare the CPR response of those materials to surrounding highland terrain and radar-facing slopes in the vicinity of the crater. The floor of Cabeus crater was also targeted at X-band on 3 occasions in the previous year and the floor of Amundsen crater was also targeted on 3 occasions. The purpose of these observations is to constrain the depth to and thickness of materials with similar scattering characteristics.

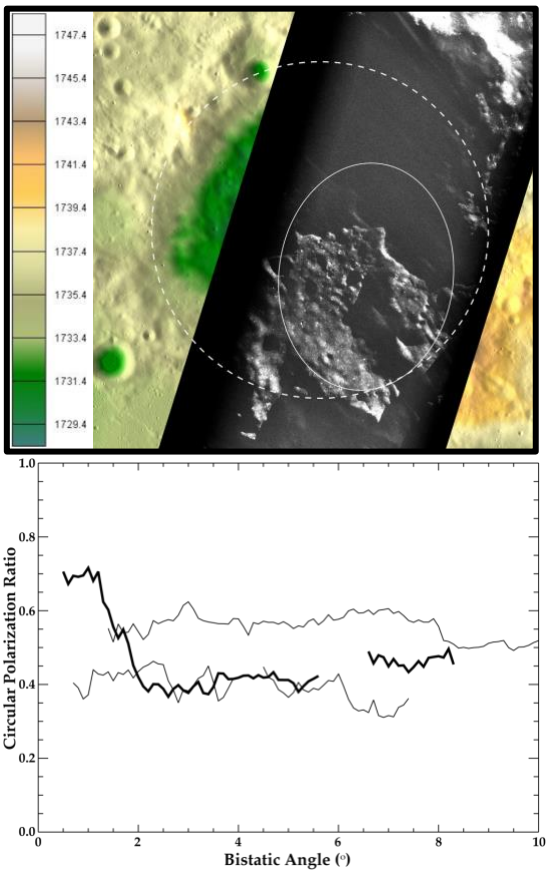

Figure 1: *(above) Portion of backscatter data for S-band bistatic observation 2013-346, overlain on LOLA topographic information (scale shown in km of radius). Dashed circle represents approximate location of crater rim and solid oval represents approximate area sampled in all bistatic observations of the crater floor. (below) Plot of mean CPR versus bistatic angle for Cabeus floor materials sampled in 5 bistatic observations targeting Cabeus at incidence angles ranging from 82.4° to 86.6° (bold line), highland materials observed at incidence angles ranging from 64° to 81.5°, (upper solid line), and radar-facing slopes observed at incidence angles ranging from 76.5° to 82° (lower solid line).*

4. Results

Mini-RF S-band observations of the floor of Cabeus cover bistatic angles of 0.5° to 8.6° for incidence angles ranging from 82.4° to 86.6° (*Fig. 1*). CPR measurements for the floor of the crater, as a function of bistatic angle, show a clear opposition surge; something not observed for the floors of nearby, similar-sized craters that were sampled at S-band wavelengths (e.g., Casatus, Klaproth, Blancanus, and Newton A and G) [1]. The opposition peak of Cabeus floor materials has a width of ~2° and features a ~30% increase in CPR. The bistatic observations of the region surrounding Cabeus indicate that mean CPR values for the portion of its floor that was imaged by Mini-RF are less than that of the surrounding highlands for bistatic angles > ~1.8° but similar to that of nearby radar-facing slopes. Mean CPR values for the imaged floor of Cabeus are higher than that of surrounding highlands and nearby radar-facing slopes for bistatic angles of 0.5° to 1.8°. Mini-RF data for bistatic angles < 0.5° were not acquired during the bistatic campaign. However, Mini-RF monostatic data (i.e., bistatic angle of 0°) of the crater floor were acquired at an incidence angle of 48° [14] and ground-based CPR measurements at a bistatic angle of 0.37° and large (> 80°) incidence angles have been made [e.g., 16]. Elevated CPRs were not observed in either case.

Mini-RF X-band observations of the floor of Cabeus cover equivalent incidence angles but a smaller range of bistatic angles than are currently sampled at S-band. Based on these observations, there is no indication of an opposition response. Data for the floor of Amundsen crater similarly does suggest an opposition response but its character is distinctly different from the S-band response observed for Cabeus. This could indicate that, if water ice is present in Cabeus crater floor materials, it is buried beneath ~0.5 m of regolith that does not include radar-detectible deposits of water ice.

References

[1] Patterson et al., 2017, Icarus, 283, 2-19; [2] Campbell et al. (2010), Icarus, 208, 565-573; [3] Raney et al. (2012), JGR, 117, E00H21; [4] Carter et al. (2012), JGR, 117, E00H09; [5] Campbell (2012), JGR, 117, E06008; [6] Hapke et al. (2012), JGR, 117, E00H15, doi:10.1029/2011JE003916; [7] Nelson et al. (2000), Icarus, 147, 545-558; [8] Piatek et al. (2004), Icarus, 171, 531-545. [9] Hapke and Blewett (1991), Nature, 352, 46-47; [10] Mishchenko (1992), Astrophys. and Space Sci., 194, 327-333; [11] Mishchenko (1992), Earth, Moon, and Planets, 58, 127-144; [12] Spudis P.D. et al. (2010) GRL [13] Spudis et al. (2013), JGR 118, 1-14; [14] Neish et al., 2011, JGR (Planets), 116, E01005, doi:10.1029/2010JE003647; [15] Patterson et al., 2013, 44th LPSC, #2380; [16] Campbell et al., 2006, Nature 443, 835-837.

EPSC Abstracts
Vol. 12, EPSC2018-1028, 2018
European Planetary Science Congress 2018

In-situ analysis of lunar regolith with the gas chromatograph-neutral gas mass spectrometer on the Luna-Resurs lander

R.G. Fausch (1), P. Wurz (1), D. Lasi (1), M. Tulej (1), M. Cabane (2), C. Szopa (2), A. Sapgir (3) and M. Gerasimov (3)
(1) University of Bern, Physics Institute, Space Research and Planetary Sciences, Switzerland, (2) LATMOS, Université Pierre et Marie Curie, 75252 Paris, France, (3) Space Research Institute IKI, Profsoyuznaya 84/32, 117997 Moscow, Russia (rico.fausch@space.unibe.ch)

Abstract

We developed a time-of-flight neutral gas mass spectrometer (NGMS) that was selected as part of the gas analytic package for the Luna-Resurs mission to investigate lunar regolith and the lunar exosphere in-situ. The recently presented scientific performance measurements of the NGMS prototype [4] are comparable with preliminary calibration data of the flight model. Hence, NGMS will fully comply with the scientific requirements of the Luna-Resurs mission.

1. Introduction

Analysing chemical composition of the volatile species in lunar soil has contributed significantly to our understanding of the origin and evolution of the Moon and solar system bodies but key questions remain unanswered. Volatiles and water are shown to be present on the lunar polar regions [2] but the absence of highly sensitive in-situ chemical composition measurements only allow for speculations about how the Moon evolved. Therefore, chemical analysis of lunar regolith is of considerable interest in the Russian Luna-Resurs mission.

2. NGMS

The NGMS instrument [3, 7] design benefits from heritage from P-BACE/MEAP [1] and RTOF/ROSINA/Rosetta [6] instruments. Analysis capabilities of the instrument include investigation of volatiles and their chemical composition, the fraction of water and organic compounds as well as isotope composition of CHON and noble gases, and its scientific performance depends on the measurement mode and the mission phase respectively.

Figure 1: Mass of the NGMS flight model is < 3.5 kg, size is 18 x 26 x 15 cm^3 and it consumes < 25 W [3].

2.1 GC

The NGMS instrument operates with pyrolysis cells with temperatures of up to 1100°C to release volatiles from the collected regolith sample, a thermal analyser and a gas chromatograph (GC) are used for chemical pre-separation. The continuous analysis of the GC outflow allows for a dynamic range of up to 10^6 within 1 second integration time.

Prototype GC-NGMS measurements show sensitivities of hydrocarbons of about $2 \cdot 10^{-10}$ by mass and of about $2 \cdot 10^{-9}$ by mass for noble gases [4]. Measurements with the NGMS flight model and

prototype GC columns indicate that a similar range as in the NGMS prototype measurements is feasible during the mission. For comparison, for the SAM instrument, the GC-mass spectrometer on the Curiosity rover of NASA, the reported sensitivity for organic compounds is $(1–10)\cdot10^{-9}$ by mass [5].

2.1 Exosphere

During cruise phase and on the surface, NGMS analyses the tenuous exosphere as a stand-alone instrument with an increased signal-to-noise ratio compared to the GC mode due to higher integration times. Calibration measurements with noble gas mixtures show that the instrument is able increase its dynamic range which is mainly limited by the mission scenario (integration time) while the mass resolution is still up to $m/\Delta m = 1200$. Trace gas quantities of species at 10^{-16} mbar partial pressure could therefore be measured when assuming an ambient gas pressure of the lunar atmosphere in the order of 10^{-10} mbar [7].

3. Summary and conclusion

We developed a neutral gas mass spectrometer which operates as a stand-alone device or in combination with a gas chromatograph. In both cases the NGMS instrument is capable to analyse both the structure and composition of molecules, isotopes and elements. The dynamic range of the flight instrument is estimated to be in a similar range as the reported prototype levels which is about 6 decades within 1 second integration time allowing for highly sensitive isotope and chemical composition analysis of the lunar surface and exosphere.

Acknowledgements

This work is supported by the Swiss Space Office through the ESA PRODEX program and by the Swiss National Science Foundation.

References

[1] Abplanalp, D. et al.: A neutral gas mass spectrometer to measure the chemical composition of the stratosphere, Adv. Space Res., Vol. 44, pp. 870–878, 2009.

[2] Colaprete, A. et al.: Detection of water in the LCROSS ejecta plume, Science, Vol. 330, pp. 463–468, 2010.

[3] Fausch, R. et al.: Flight electronics of GC-mass spectrometer for investigation of volatiles in the lunar regolith, IEEE Aerospace Conference, in press, 2018.

[4] Hofer, L. et al.: Prototype of the gas chromatograph–mass spectrometer to investigate volatile species in the lunar soil for the Luna-Resurs mission, Planetary and Space Science, Vol. 111, pp. 126–133, 2015.

[5] Mahaffy, P. et al.: The sample analysis at mars investigation and instrument suite, Sp. Sci. Rev., Vol. 170, pp. 401–478, 2012.

[6] Scherer, S. et al.: A novel principle for an ion mirror design in time-of-flight mass spectrometry, Int. Jou. Mass Spectr. Vol. 251, pp. 73–81, 2006.

[7] Wurz, P. et al.: A neutral gas mass spectrometer for the investigation of lunar volatiles, Planetary and Space Science, Vol. 74, pp. 264–269, 2012.

EPSC Abstracts
Vol. 12, EPSC2018-1071, 2018
European Planetary Science Congress 2018

Lunar Science, Volatiles Prospecting and In-Situ Resource Utilisation: Synergistic Science and Exploration

S. J. Barber; F. Abernethy, M. Anand, V. Levin-Prabhu, S. Lim, A.D. Morse, J. Mortimer, C. Pitcher, H. Sargeant, S. Sheridan, A. Verchovsky, I.P. Wright

The Open University, Milton Keynes, UK. simeon.barber@open.ac.uk

Abstract

A host of new missions to the surface of the Moon are in preparation internationally. A key objective is to perform in-situ investigations of putative water ice and other volatiles, and determine their abundance and extractability for future In-Situ Resource Utilisation (ISRU). This paper describes how a range of existing and developing technologies and techniques may be applied for the benefit of lunar science and exploration.

1. Introduction

The Open University (OU) has been a key player in lunar science since the Apollo era, with activities spanning from analysis of returned samples to in-situ instrumentation, and from scientific- to exploration-motivated research in volatiles and other potential resources in and on the Moon [Anand, 2010; Anand et al., 2012; 2014].

Initial interests were in the development and application of specialised mass spectrometers for stable isotopic studies of Apollo, Luna and meteorite samples. As a natural progression, OU since started a programme of miniaturising these instruments for flight on major space missions including the Rosetta comet investigation [Wright et al., 2015; Morse et al. 2015] and the ExoMars 2020 Surface Platform.

Investigations of lunar volatiles, whether motivated by scientific or exploration objectives, can be addressed through a combination of the above experience and capabilities. The miniature science laboratory ProSPA [Barber et al., 2018a] is being developed for the prospecting and analysis of lunar ices and chemically/physically-sorbed volatiles within the PROSPECT package for the Luna-27 lander (Roscosmos/ESA). It combines elements of earlier space instruments to replicate laboratory-based analytical protocols that have previously been applied to returned lunar samples and meteorites. These experiments can therefore be performed in-situ on the Moon on freshly drilled samples in new locations, with the results being valuable both in themselves and as context for the wealth of existing sample analysis data in the literature.

Further instrument and mission concepts are in development for science and resource prospecting from rovers [Biswas et al., 2018] and penetrators [Barber et al., 2018b].

OU is also preparing for the transition from prospecting for lunar resources, to developing a new sustainable mode of space exploration based on the utilisation of local resources (ISRU). Activities in this area range from chemical processes for the extraction of oxygen from lunar regolith [Sargeant et al., 2018] to microwave processing for additive manufacturing (3D-printing) of lunar materials [Lim et al., 2017; Srivastava et al., 2016].

This presentation will describe current and developing capabilities, interests and aspirations and how these are being applied in the context of European and international plans for lunar science and exploration. The potential synergies between in situ science and laboratory analysis of new returned samples will be explored, with a view to science and exploration advancing together for mutual benefit.

References

[1] Anand, Mahesh (2010). Lunar water: a brief review. Earth Moon and Planets, 107(1) pp. 65–73.

[2] Anand, M.; Crawford, I. A.; Balat-Pichelin, M.; Abanades, S.; van Westrenen, W.; Péraudeau, G.; Jaumann, R. and Seboldt, W. (2012). A brief review of chemical and mineralogical resources on the Moon and likely initial in situ resource utilization (ISRU) applications. PSS, 74(1) pp. 42–48.

[3] Anand, Mahesh; Tartèse, Romain and Barnes, Jessica (2014). Understanding the origin and evolution of water in the Moon through lunar sample studies. Phil. Trans. A, 372(2024)

[4] Barber, S. J. et al. (2018a) ProSPA: Analysis of Lunar Polar Volatiles and ISRU Demonstration on the Moon, LPSC 2018, The Woodlands, Texas, https://www.hou.usra.edu/meetings/lpsc2018/pdf/2172.pdf .

[5] Barber, S. J. et al. (2018b) L-DART: a Penetrator Mission for Lunar Permanently Shadowed Regions, LPSC 2018, The Woodlands, Texas, https://www.hou.usra.edu/meetings/lpsc2018/pdf/2941.pdf

[6] Biswas, J. et al. (2018) Mobile In-Situ Exploration Of Lunar Volatiles With The LVS On LUVMI, European Lunar Symposium, https://els2018.arc.nasa.gov/downloads/ELS_2018_Abstract_Booklet_08052018.pdf

[7] Lim, S., Levin Prabhu, V., Anand, M., Taylor, L., (2017), "Extra-terrestrial construction processes - advancements, opportunities and challenges", Advances in Space Research Journal, Vol 60, Issue 7, pp. 1413-1429. https://dx.doi.org/10.1016/j.asr.2017.06.038 Corrigendum: https://dx.doi.org/10.1016/j.asr.2018.03.022

[8] Morse, A.; Moussis, O.; Sheridan, S.; Morgan, G.; Andrews, D.; Barber, S. and Wright, I. (2015). Low CO/CO2 ratios of comet 67P measured at the Abydos landing site by the Ptolemy mass spectrometer. Astronomy & Astrophysics, 583, article no. A42

[9] Sargeant, H. M. et al. Hydrogen reduction of ilmenite in a static system for a lunar ISRU demonstration. European Lunar Symposium, https://els2018.arc.nasa.gov/downloads/ELS_2018_Abstract_Booklet_08052018.pdf

[10] Srivastava, V., Lim, S., Anand, M., (2016), "Microwave processing of lunar soil for supporting longer-term surface exploration on the Moon", Special Issues, Space Policy Journal, Vol 37, Issue 2, pp. 92-96. http://dx.doi.org/10.1016/j.spacepol.2016.07.005

[11] Wright, I. P.; Sheridan, S.; Barber, S. J.; Morgan, G. H.; Andrews, D. J. and Morse, A. D. (2015). CHO-bearing organic compounds at the surface of 67P/Churyumov-Gerasimenko revealed by Ptolemy. Science, 349(6247)

EPSC Abstracts
Vol. 12, EPSC2018-1091, 2018
European Planetary Science Congress 2018

Far-IR Emissivity in Lunar South Polar Permanently Shaded Terrain: Apparent Temperature Dependence

Elliot Sefton-Nash (1), Jean-Pierre Williams (2), Joshua Bandfield (3), Tristram Warren (4), Benjamin T. Greenhagen (5) and, David A. Paige (2).
(1) ESTEC, European Space Agency, Keplerlaan 1, Noordwijk 2201AZ, Netherlands (e.sefton-nash@cosmos.esa.int) (2) Department of Earth, Planetary and Space Sciences, University of California Los Angeles, CA, USA. (3) Space Science Institute, Boulder, CO, USA. (4) Department of Physics, University of Oxford, UK. (5) Applied Physics Laboratory, Johns Hopkins University, Baltimore, MD, USA.

1. Introduction

The northern floor and wall of Amundsen crater, near the lunar south pole, is a permanently shadowed region. We report on interpretation of results from observations of two targets on the floor of Amundsen, one in the permanently shadowed region (PSR) and the other in the partially illuminated area (NPSR) (Figure 1), with the goal of observing relative differences in their far-IR emissivity in nighttime observations by LROs Diviner Lunar Radiometer Experiment. A 3km radius around centers of 93.1047°E, 84.5523°S and 91.2826°E, 83.6889°S define the NPSR and PSR targets, respectively.

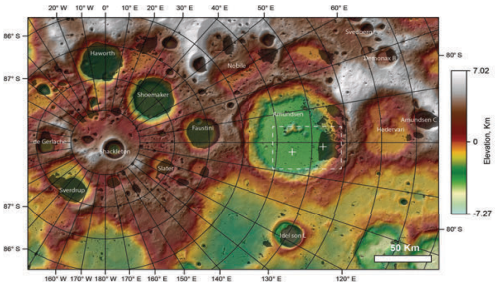

Figure 1: Study area and targets: colorized hillshade from LOLA 20m/pix data. Regions in permanent shadow darkened using 120 m/pixel map [1]. Dashed box contains 2 targets in Amundsen crater marked with white '+'s.

The permanently shadowed target includes terrain that is reported to indicate generally brighter 1064 nm albedo combined with annual maximum surface temperatures low enough to enable persistence of surface water ice (< 110K). Many permanently shadowed areas with similar LOLA reflectance characteristics do not show this trend [2].

This is consistent with a similar correlation of annual maximum temperature with anomalous ultraviolet radiation as measured by the LAMP instrument [3]. A patchy distribution of areas in the PSR target show a combination of off/on-band ratios > 1.2 and Lyman-α albedo < 0.03, indicating a possible water mass content of 0.1 – 2.0% [4].
Portions of our PSR target therefore indicate annual maximum temperatures, as well as ultraviolet and near-IR signatures that are anomalous compared to other south polar terrain in permanent shadow, consistent with the presence of surface water frost.

Indeed, our intent in previous work was to determine if the presence of water frost could be verified through study of far-IR emissivity trends, near the planck peak at PSR temperatures.

2. Method

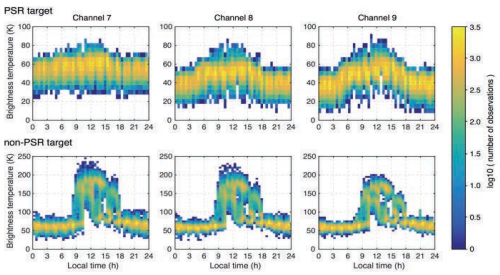

Figure 2: Brightness temperatures observed for PSR (top) and NPSR (bottom) targets between Jul. 2009 – Aug. 2017) plot over local mean solar time (LMST).

To quantify deviations in observed emissivity from what would be expected from planck emission, we model the band ratio of channels 8 and 9 ($\Re_{8/9}$) as a function of surface temperature, because these long wavelength channels are most sensitive to PSR-relevant temperatures. This model allows us to plot the tentative signature of changes in apparent emissivity as a function of surface temperature, without assuming a value for emissivity.
After differencing the model with observations as a function of bolometric brightness temperature (T_{BOL}: the channel-integrated best estimate of surface kinetic temperature), we previously asserted that the offset in $\Re_{8/9} - \Re_{8/9model}$ for the PSR target and its apparent temperature dependence at temperatures < 40 K, may indicate different thermophysical gradients between

the targets, perhaps attributed to surface layers, including surface water frost.

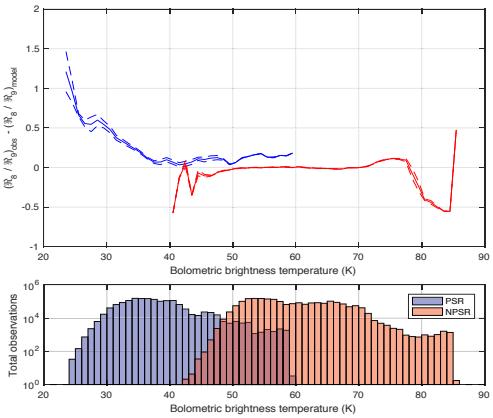

Figure 3: Band ratio model vs observations ±1σ over T_{BOL}.

3. Discussion

Here we update our interpretation of these results to consider the possible effects of surface roughness in PSRs. Sub-field of view (FOV) scale "micro" doubly-shadowed cold traps, topographic lows in PSRs that are also protected from secondary and higher order thermal emission (e.g. from crater walls), may contribute to anisothermality in PSRs. We construct a simple model that considers radiance contributions from a bi-modal brightness temperature distribution (Figure 4). PSR terrain is fixed at 40K, and $\mathfrak{R}_{8/9}$ is modelled as the temperature, and fraction, of doubley-shadowed PSRs is varied. Figure 4 shows the deviation of $\mathfrak{R}_{8/9}$ over these parameters from that expected from a homogenous temperature distribution at 40K. Deviation is largest when PSR and double PSR are similar in temperature (and therefore signal), but also when temperature hetereogeneity is largest. For PSR material at 40K (typical for nighttime PSR temperatures, Fig. 2), low to modest fractions (0-0.6) of micro cold traps, that are just a few K cooler than the PSR terrain, could produce the observed deviation in $\mathfrak{R}_{8/9} - \mathfrak{R}_{8/9model}$.

Apparent temperature dependence could also be explained by this mechanism, simply because there are many observations and their FOV contents do not all have the same micro double-PSR fraction.

The range of different micro-cold trap fractions in FOVs leads to a range of brightness temperatures, and degrees of ansiothermality. Colder brightness temperatures may result from larger fractions of, or colder, doubley shadowed regions within an FOV.

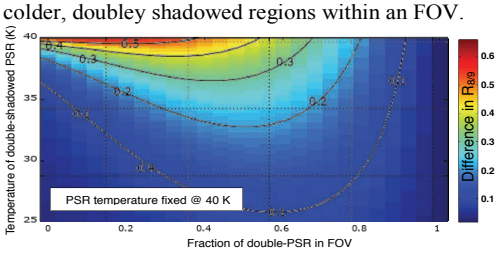

Figure 4: Magnitude of difference in $\mathfrak{R}_{8/9}$ between bi-modal and unimodal temperature distribution in a FOV on a PSR. PSR temperature fixed at 40K, and fraction of double-shadowed PSR, and its T, are varied.

4. Conclusions

The nighttime radiance ratio between Diviner channels 8 and 9, distinguishes a PSR from a non-PSR target on the floor of Amundsen crater in two ways: 1) Data for the PSR target is always positively offset from the non-PSR target, indicating that emission in channel 9 decreases relative to that in 8. 2) The effect becomes temperature dependant < 40 K, and increases with decreasing temperature. Building on previous results, we interpret that there may be two possible causes: **1)** The two targets may have different gradients in thermophysical properties due to different epiregolith structure [e.g. Mendell and Noble, 2010], possibly including surface water frost suggested in other studies. Such structure may be responsible for temperature dependant thermal conductivity [e.g. 7, 8]. **2)** The offset and temperature-dependent anisothermality for the PSR target may be attributed to sub-EFOV scale "micro" cold traps that are not resolved in the Diviner data. Using a simple model, and depending on the fraction of cold-traps in a given EFOV, these micro cold traps could be a few to several 10s of degrees K colder than the surrounding PSR.

References

[1] Marzarico et al., (2011), Icarus 211, p. 1066-1081. [2] Fisher, E. A. et al. (2017), *Icarus* 292, p. 74-85. [3] Gladstone, G. R. et al. (2012), *J. Geo. Res.* 117, E00H04. [4] Hayne, P. O. et al. (2015), Icarus 255, p. 58-69. [5] Williams, J.-P. et al., (2016), Icarus 273, p. 205-213. [6] Paige D. A. et al. (2010), Space Sci. Rev. 150, p. 125–160. [7] Woods-Robinson, R. et al. (2016) AGU, Abs. P21A-2077. [8] Siegler, M. A. et al. (2016) AGU, Abs. P24A-05.

EPSC Abstracts
Vol. 12, EPSC2018-1123, 2018
European Planetary Science Congress 2018

Observations of illumination conditions in the Permanently Shadowed Regions (PSRs) with LRO-LAMP

Kathleen Mandt (1), E. Mazarico (2), T. K. Greathouse (3), K. D. Retherford (3,4), G. R. Gladstone (3,4), B. Byron (4,3), D. M. Hurley (1), A. M. Stickle (1), G. W. Patterson (1), A. R. Hendrix (5), J.-P. Williams (6), Y. Liu (7), and M. Lemelin (8)

(1) Johns Hopkins University Applied Physics Laboratory, Laurel, MD (Kathleen.Mandt@jhuapl.edu), (2) Goddard Space Flight Center, (3) Southwest Research Institute, San Antonio, TX, (4) University of Texas at San Antonio, (5) Planetary Science Institute, Los Angeles, CA, (6) University of California at Los Angeles, (7) Lunar Planetary Institute, Houston, TX, (8) York University, Toronto, Canada.

Abstract

The south pole of the Moon is an area of great interest for exploration and scientific research because many low-lying regions are permanently shaded (PSRs) and are likely to trap volatiles for extended periods of time, while adjacent topographic highs can experience extended periods of sunlight. A primary goal of the Lunar Reconnaissance Orbiter (LRO) mission (Chin et al., 2007) is to characterize the spatial and temporal variability of water on the Moon, with a focus on the Permanently Shadowed Regions (PSRs). The physical properties of the regolith within the PSRs as well as the temporal variability of illumination are of critical importance for achieving this goal. We have compiled observations from multiple LRO instruments to conduct a comparison with far ultraviolet (FUV) observations made by the Lyman Alpha Mapping Project (LAMP; Gladstone et al., 2010) to evaluate illumination at the lunar south pole (within 5° of the pole).

References

Chin et al. (2007) SSRv, 129, 391-419.

Gladstone et al. (2010) SSRv, 150, 161-181.